CARBON ENERGY
Open Access
WILEY

Supporting Information

Micro/nano-wrinkled elastomeric electrodes enabling high energy storage performance and various form factors

*Changeun Yoo,† Seokmin Lee,† Yongkwon Song,† Woojae Chang, Moon Kyu Park, Younji Ko, and Jinhan Cho**

Experimental Section

Materials: PDMS precursors with curing agents (Sylgard 184) were supplied by Dow Corning (United States of America). TOABr and TREN were obtained from Alfa Aesar, and the other chemical reagents were purchased from Sigma-Aldrich. Organic solvents were obtained from Daejung Chemicals & Metals (Republic of Korea). All chemical reagents were used as received without further purification.

Synthesis of TOABr-Au NPs: TOABr-Au NPs were synthesized in toluene according to the Brust-Schiffrin method.[S1] In brief, a 30 mM solution of $HAuCl_4 \cdot 3H_2O$ in deionized water (30 mL) was added to a 25 mM solution of TOABr ligands in toluene (80 mL). After the transfer of metal salts from deionized water to toluene, a freshly prepared 0.4 M solution of $NaBH_4$ in deionized water (25 mL) was added to the stirred mixture, resulting in an immediate reduction. After 3 h, the isolated toluene phase was washed with 0.1 M H_2SO_4, 0.1 M NaOH, and deionized water several times using a separate funnel to obtain TOABr-Au NPs in toluene.

Preparation of SH-PDMS: For the preparation of SH-PDMS, we first prepared a PDMS prepolymer mixture of precursor and cross-linking curing agent in a weight ratio of 10:1. The bubbles generated from the prepolymer mixture were removed in a vacuum chamber for 2 h. The prepolymer mixture was poured onto fluorosilanized Si wafers with a uniform thickness using doctor-blade process and cured at 150 °C for 15 min to obtain PDMS film. Then, the peeled PDMS film was thiolated as described by Brook and coworkers.[S2] Briefly, the PDMS film was immersed into a mixture solution of (3-mercaptopropyl)trimethoxysilane (2.65 mL) and methanol (28 mL) containing KOH (0.28 g) in an ultrasonic bath for 6 h at 50 °C. After that, the surface-treated PDMS film was washed with dichloromethane to acquire SH-PDMS.

Preparation of Au NP-PDMS and Ni-PDMS: For the preparation of ECC (Ni-PDMS), metal

NP assembly onto SH-PDMS was preceded for the formation of conductive seed layer for subsequent electrodeposition. The SH-PDMS was dipped into a toluene solution of TOABr-Au NPs (5 mg mL^{-1}) for 30 min and washed with pure toluene to remove weakly adsorbed NPs. Next, the TOABr-Au NP-coated PDMS was dipped into an ethanol solution of TREN (1 mg mL^{-1}) for 15 min and washed with pure ethanol, resulting in the formation of (TOABr-Au NP/TREN)$_{n = 1}$/PDMS. This deposition cycle of TOABr-Au NPs and TREN was repeated to produce (TOABr-Au NP/TREN)$_{n = 2}$/PDMS (Au NP-PDMS) with an electrical conductivity of ~580 S cm^{-1}. Sequentially, the prepared conductive Au NP-PDMS was immersed into a typical Watt bath (45 g L^{-1} of $NiCl_2$, 240 g L^{-1} of $NiSO_4$, and 30 g L^{-1} of H_3BO_3) based on a two-electrode system with a high-purity Ni plate as a counter electrode.[S3] The electrodeposition of Ni was carried out at a current density of 20 mA cm^{-2} for 1 min, followed by washing with pure deionized water and drying at room temperature, which resulted in the Ni-PDMS.

Preparation of NiCo-PDMS: ECC-based energy storage electrodes (NiCo-PDMS) were prepared by the electrodeposition of NiCo onto Ni-PDMS in a standard three-electrode system (consisting of Ni-PDMS as a working electrode, Pt coil as a counter electrode, and Ag/AgCl electrode as a reference electrode) using an aqueous electrolyte (10 mM $NiSO_4 \cdot 6H_2O$ and 5 mM $Co(NO_3)_2$ in 50 mL of deionized water).[S4] Resultantly, the NiCo-PDMS was produced after electrodeposition at a current density of 1 mA cm^{-2} for 5 min, washing with pure deionized water, and drying at room temperature.

Preparation of NiCo-PU: The experimental procedure for the preparation of NiCo-PU was the same as that of NiCo-PDMS; however, amine-functionalized PU (NH_2-PU) was used instead of SH-PDMS. The NH_2-PU was acquired by dipping PU film into an ethanol solution of poly(ethyleneimine) (PEI, 1 mg mL^{-1}, M_w of ~800 g mol^{-1}), followed by washing with pure ethanol to remove weakly adsorbed materials.

Preparation of Spiral-Structured PDMS: A screw with a helix angle of ~20° and a pitch of ~2.5 mm was used as a mold for the preparation of spiral-structured PDMS.[S5] PDMS prepolymer mixture (weight ratio of precursor and curing agent = 10:1) was filled in the straw without any bubbles. Then, the screw was inserted into the prepolymer mixture-filled straw by tightening the screw, followed by curing at 150 °C for 15 min. After curing, the spiral-structured PDMS was obtained by carefully peeling it off from the screw.

Preparation of Porous-Structured PDMS: Porous-structured PDMS was fabricated as previously reported in the literature with slight modification,[S6] using a commercial Ni foam with a thickness of ~1 mm as a mold. A PDMS prepolymer mixture (weight ratio of precursor and curing agent = 10:1) and ethyl acetate (as a solvent) were well-blended using a vortex for 30 min to dilute the prepolymer mixture. The Ni foam was coated with the diluted prepolymer mixture, stored in a vacuum chamber for 30 min at room temperature to remove bubbles trapped in the pores, and cured at 100 °C for 1 h. After curing, the formed PDMS-coated Ni foam was dipped in a HCl solution to selectively etch the Ni foam for 48 h. Finally, the porous-structured PDMS was immersed into deionized water for 24 h to clean the etchant residues and dried at room temperature.

Preparation of Spherical PDMS with Intaglio Patterns: A PDMS prepolymer mixture (weight ratio of precursor and curing agent = 10:1) was poured onto a steel ball with a diameter of 2 cm without any bubbles and then cured at 150 °C for 15 min. After curing, dry powder of polystyrene (PS) colloids with a diameter of 1 μm was mechanically rubbed onto the PDMS-coated steel ball using another PDMS film, resulting in the formation of hexagonally packed colloidal arrays. This PS-embedded spherical PDMS film acted as the template surface for the preparation of spherical PDMS with intaglio patterns. That is, the PDMS prepolymer mixture was poured onto the template surface and cured under the same conditions. Resultantly, the

spherical PDMS with intaglio patterns was acquired by soaking it in toluene to completely dissolve PS colloids.[S7,S8]

Characterization: The size/shape and crystal structure of TOABr Au-NPs was observed by HR-TEM (Tecnai 20, FEI). The ligand exchange reaction during the assembly of (TOABr-Au NP/TREN)$_n$ multilayers on Au-sputtered Si wafers was confirmed by FTIR analysis using a Cary 600 (Agilent Technologies) in an advanced grazing angle (AGA) specular mode that could detect the signal of the outermost monolayer. In this case, the obtained FTIR spectra were plotted after smoothing and baseline correction using a spectral analysis software (OMNIC, Thermo Fisher Scientific). The qualitative and quantitative growth of (TOABr-Au NP/TREN)$_n$ multilayers was monitored by UV-vis spectroscopy (Lambda 365, Perkin Elmer) and quartz crystal microbalance (QCM 200, SRS) using the Sauerbrey equation, respectively. The surface morphologies of the elastomers were investigated using FE-SEM (S-4800, Hitachi) equipped with EDX and AFM (XE-100, Park System) with a tapping mode. The water contact angle was observed using a sessile drop method by a Phoenix-300 instrument (SEO Corp.). The electrical properties of the elastomers were examined by a semiconductor parametric analyzer (Agilent 4155B, Agilent Technologies) using a two- or four-probe method. The specific surface area of the elastomers was estimated from BET analysis via N_2 gas (99.999%) adsorption at 77 K using a Quadrasorb evo (Quantachrome). XRD and XPS analyses of the elastomers were conducted using a SmartLab (Rigaku) with Cu K_α radiation and X-tool (ULVAC-PHI) with Al K_α radiation, respectively.

Electrochemical Measurements: All electrochemical measurements were conducted using an Ivium-n-Stat (Ivium Technologies) at room temperature. In the case of a three-electrode system, Hg/HgO electrode (saturated with 1 M NaOH in deionized water) and Pt mesh were used as reference and counter electrodes, respectively. In the case of a two-electrode system, a carbon

textile (CT) with a thickness of ~520 μm were used as a counter electrode. The concentrations of aqueous KOH electrolyte were 1 M (for flat/spiral NiCo-PDMS) and 6 M (for porous NiCo-PDMS), where different electrolyte concentrations were used due to the large difference in the active surface area of the electrodes. The CV and EIS analyses were conducted in a potential window from 0 to 0.6 V (*vs.* Hg/HgO reference) and in a frequency range from 10^5 to 0.1 Hz, respectively. The capacities of the electrodes were calculated from the GCD curves according to the following equation:[S9]

$$\text{Capacity} = \frac{I\Delta t}{S} \quad (1)$$

where I and Δt are the applied current and discharging time, respectively. Additionally, the variable (S) indicates the area of working electrodes (for areal capacity) and the mass loading of active components (for gravimetric capacity). The energy density (E) and power density (P) of full-cell devices were evaluated from the GCD curves according to the following equations:[S9]

$$\text{Energy density } (E) = \frac{C\Delta V^2}{7200} \quad (2)$$

$$\text{Power density } (P) = \frac{E \times 3600}{\Delta t} \quad (3)$$

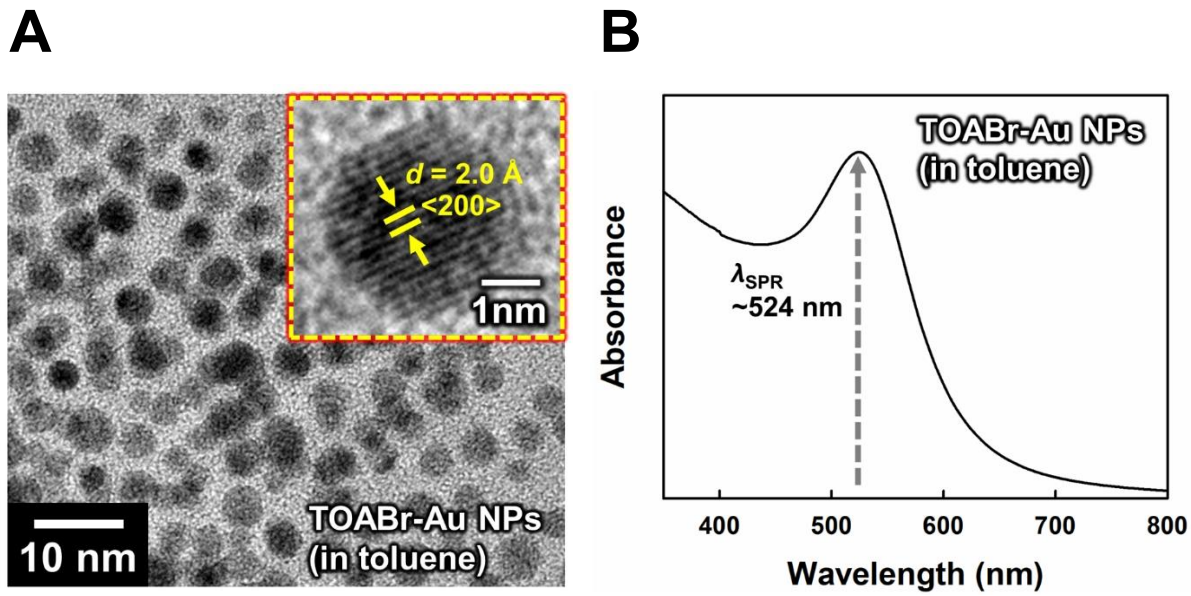

Figure S1. (A) HR-TEM images of TOABr-Au NPs (in toluene) with an average diameter of ~8 nm. The inset indicates the lattice fringe (*d*) of ~2.0 Å, which corresponded to the (200) plane of Au crystalline. (B) UV-vis spectrum of TOABr-Au NPs (in toluene) with a surface plasomon absorption peak (λ_{SPR}) of ~524 nm.

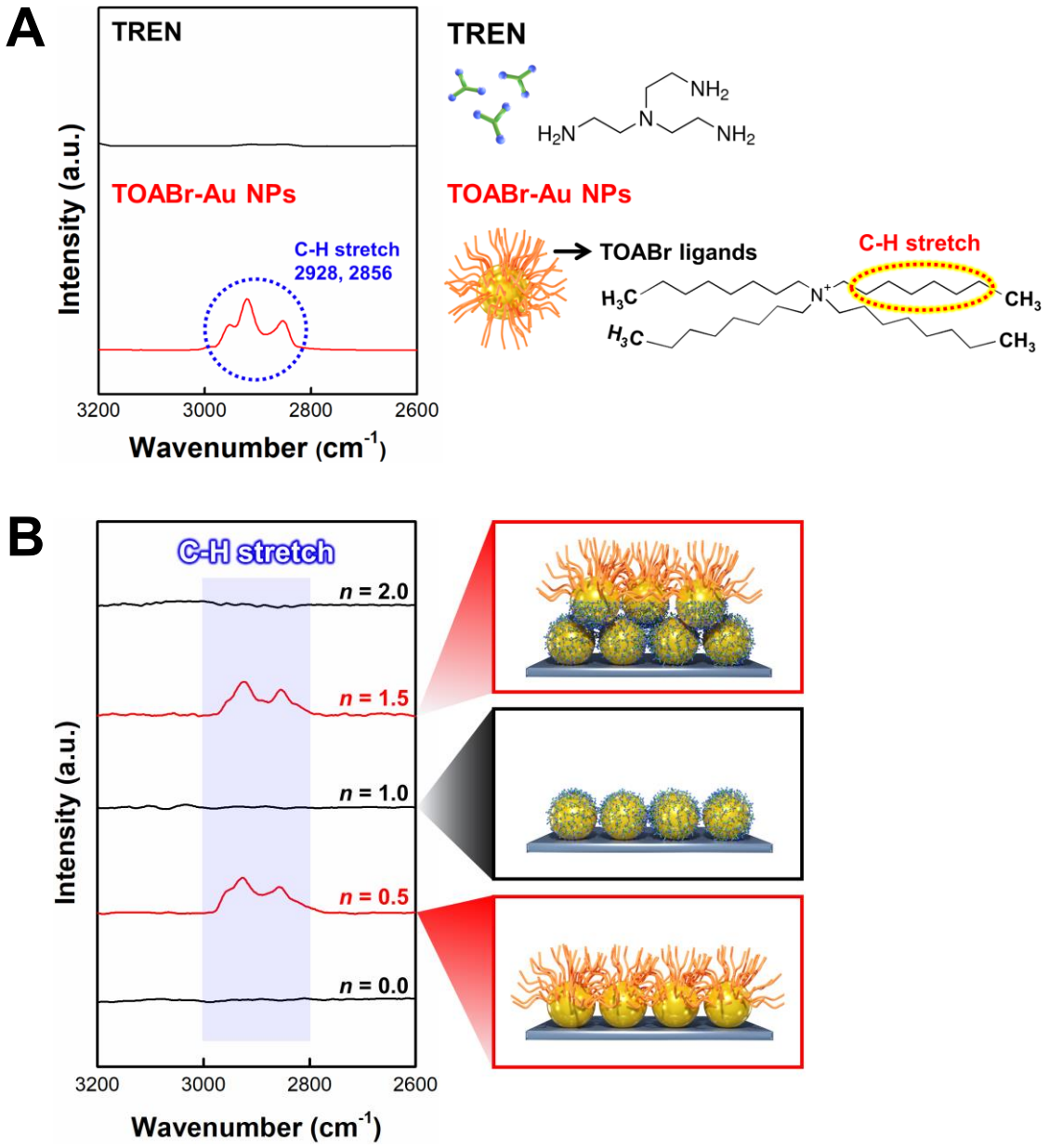

Figure S2. (A) FTIR spectra and schematic illustration of prisitne TOABr-Au NPs and TREN. The molecular structures of native TOABr ligands and TREN are also shown. (B) FTIR spectra and schematic illustration during the metal NP assembly of (TOABr-Au NP/TREN)$_n$ bilayers. As confirmed in the FTIR spectra, the C-H stretching peaks (in the range of 3000 to 2800 cm^{-1}) derived from the native TOABr ligands repeatedly generated and disappeared according to the depostion of TOABr-Au NPs and TREN, clearly proving the effective ligand exchange between the bulky/insulating TOABr ligands and the small TREN molecules on the surface of Au NPs.

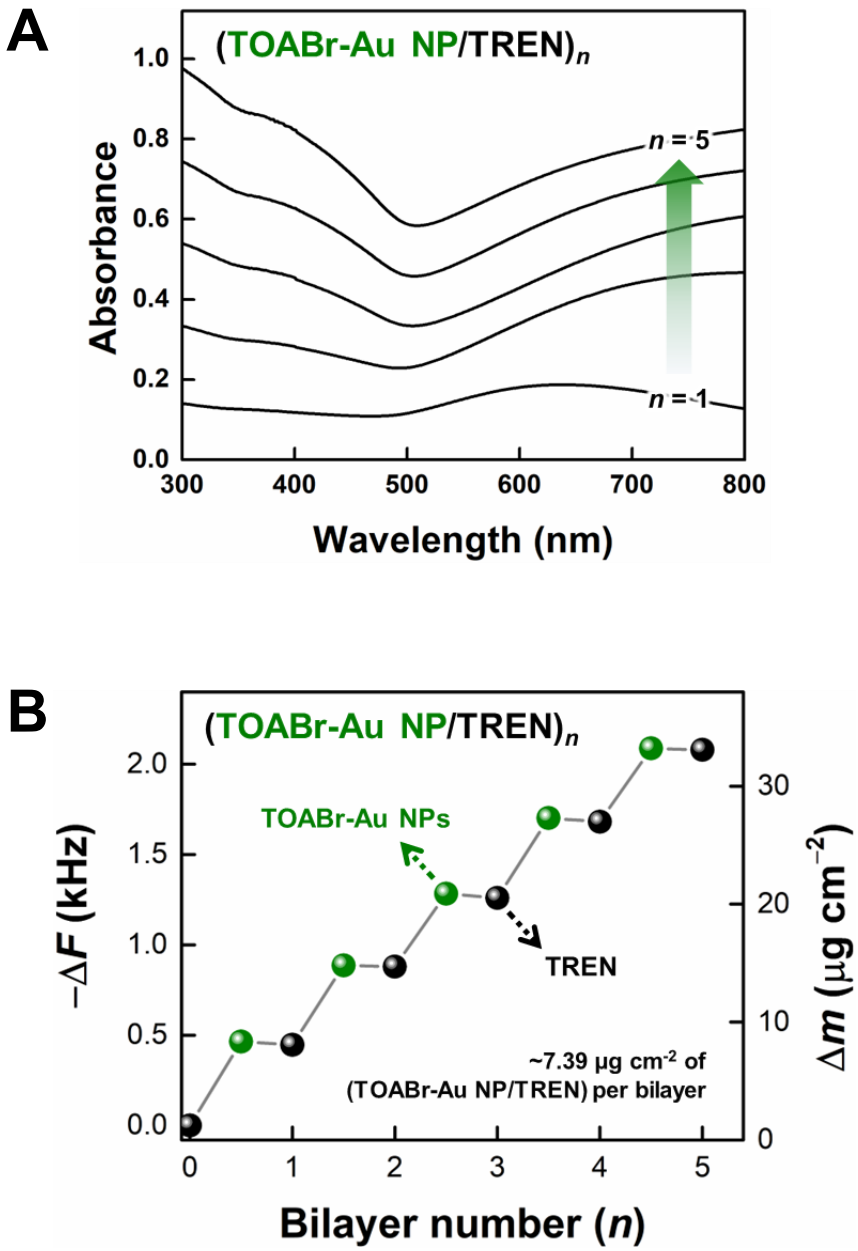

Figure S3. (A) UV-vis absorbance spectra and (B) QCM analysis of (TOABr-Au NP/TREN)$_n$ multilayers with increasing the bilayer number (n) from 0 to 5. As shown in **Figure S1B** and **S3A**, the characteristic surface plasmon resonance peak (λ_{SPR} ~524 nm in toluene) of TOABr-Au NPs was significantly red-shifted, and then disappeared with increasing the bilayer number of multilayers, indicating the drastically reduced separation distance between vertically adjacent Au NP layers.

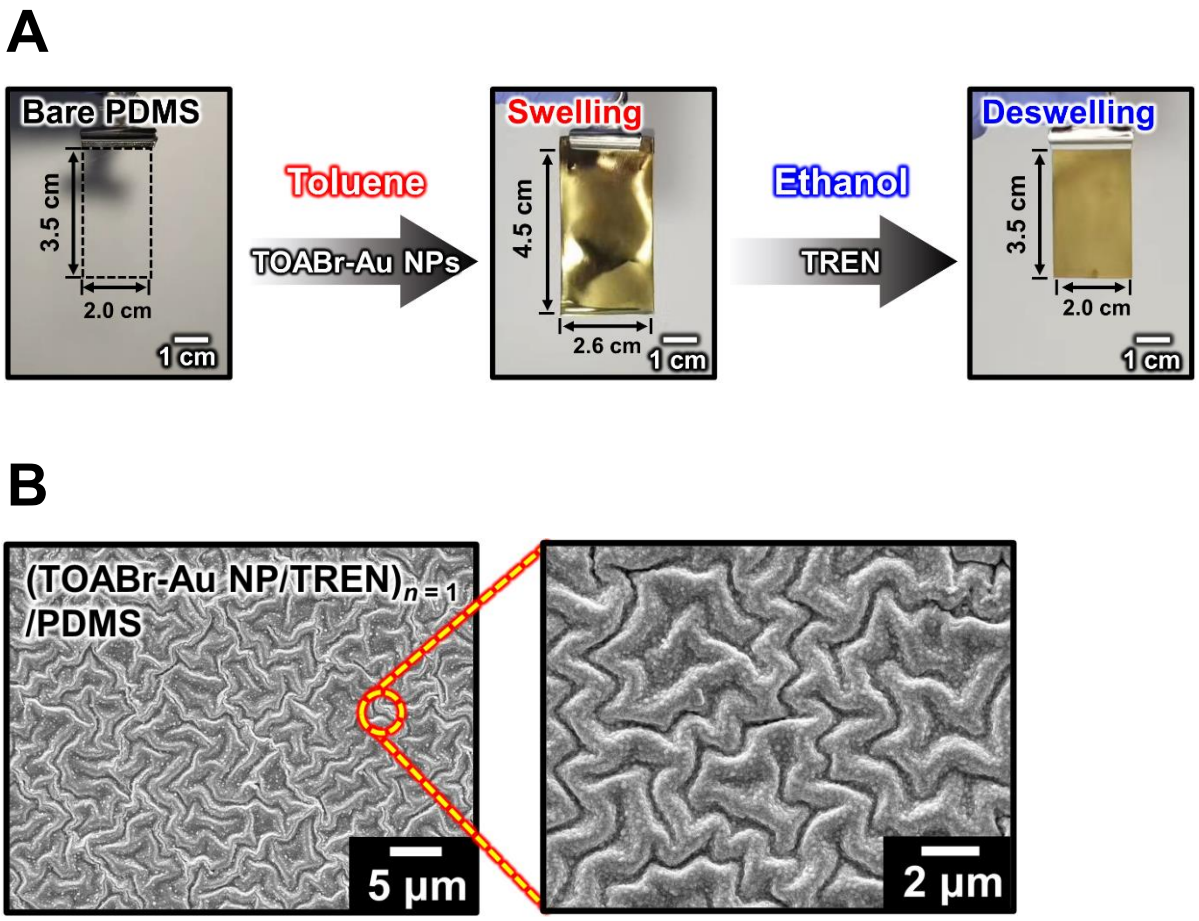

Figure S4. (A) Photographs of PDMS during the sequential of depostion of TOABr-Au NPs (on the swollen PDMS in toluene) and TREN (on the deswollen PDMS in ethanol). (B) Planar FE-SEM images of $(TOABr\text{-}Au\ NP/TREN)_{n=1}$/PDMS.

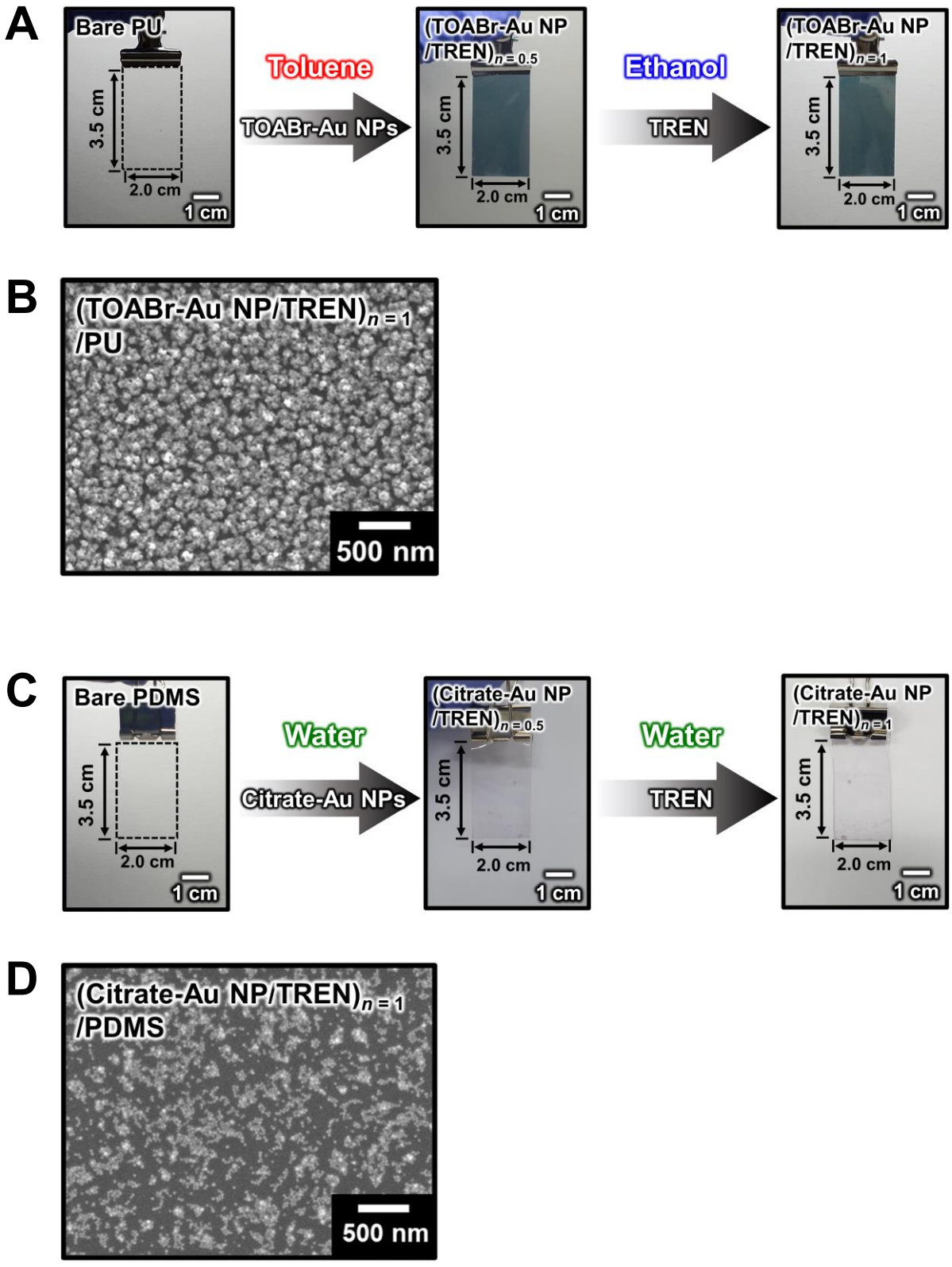

Figure S5. (A) Photographs of PU during the sequential of depostion of TOABr-Au NPs (in toluene) and TREN (in ethanol) on the non-swollen PU elastomer. (B) Planar FE-SEM iamge

of (TOABr-Au NP/TREN)$_{n = 1}$/PU. (C) Photographs of PDMS during the sequential of depostion of citrate acid-stabilized Au NPs (Citrate-Au NPs; in water) and TREN (in water) on the non-swollen PDMS elastomer. In this case, the anionic Citrate-Au NPs (in water) were prepared following the previously reported protocol.[S10] (D) Planar FE-SEM iamge of (Citrate-Au NP/TREN)$_{n = 1}$/PDMS. Comparing to the (TOABr-Au NP/TREN)$_{n = 1}$/PDMS (see **Figure S3**), the resultant (TOABr-Au NP/TREN)$_{n = 1}$/PU and (Citrate-Au NP/TREN)$_{n = 1}$/PDMS did not exhibit any micro-wrinkled structure due to the non-swollen elastomers during the assembly of metal NPs. Furthermore, the (Citrate-Au NP/TREN)$_{n = 1}$/PDMS displayed a low packing density, caused by the reciprocal electrostatic repulsion between the charged Au NPs.

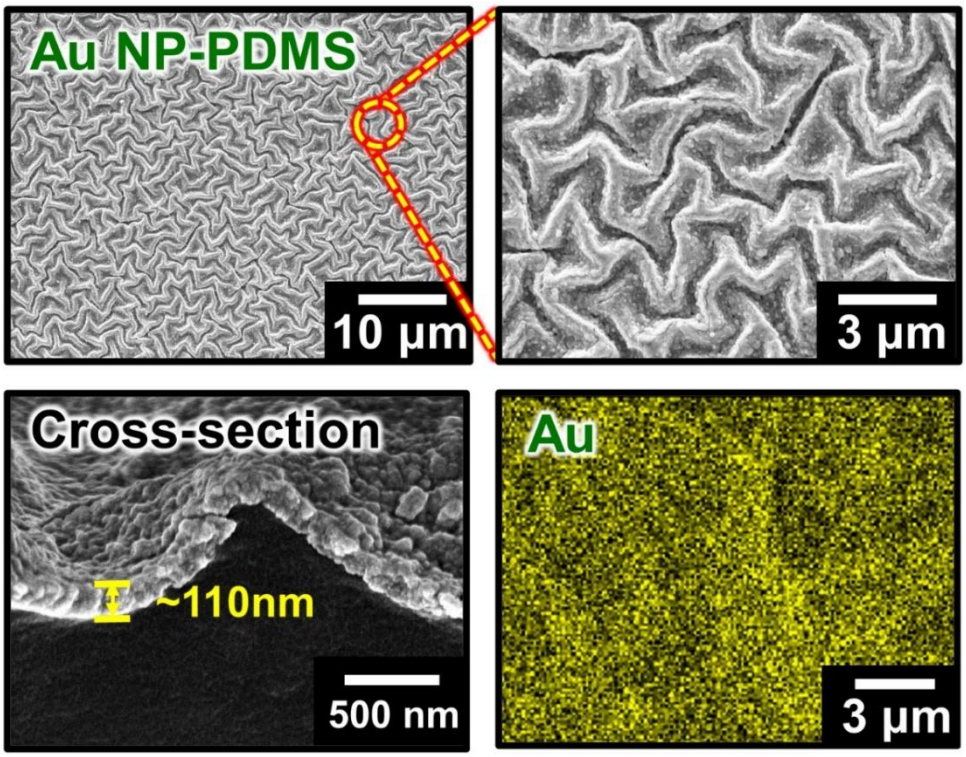

Figure S6. Planar (top side) and cross-sectional (bottom left side) FE-SEM images with EDX elemental mapping (Au) of (TOABr-Au NP/TREN)$_{n = 2}$/PDMS (Au NP-PDMS).

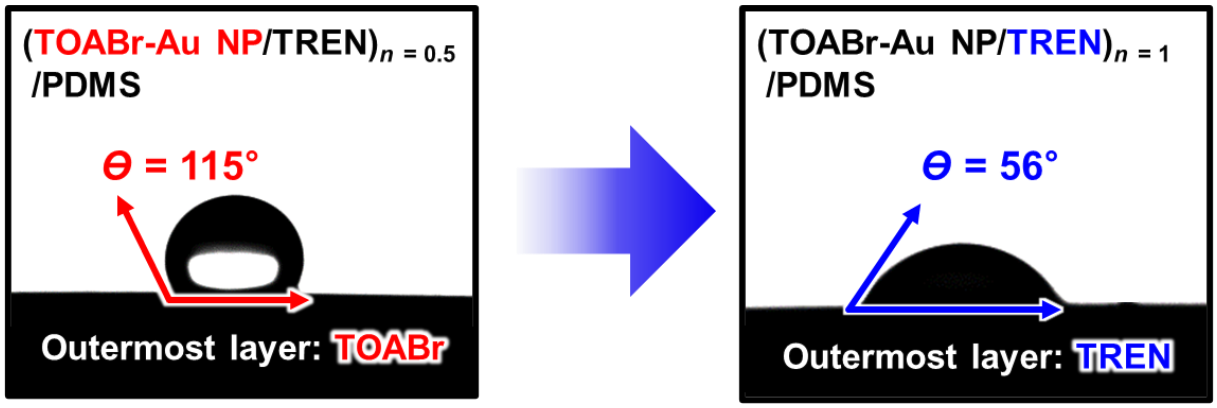

Figure S7. Photographs of water droplets with contact angles (θ) of (TOABr-Au NP/TREN)$_{n = 0.5}$/PDMS and (TOABr-Au NP/TREN)$_{n = 1}$/PDMS. As a result, the outermost TREN-coated (TOABr-Au NP/TREN)$_{n = 1}$/PDMS exhibited hydrophilic surface properties with a relatively lower contact angle of 56° compared to the outermost TOABr-coated (TOABr-Au NP/TREN)$_{n = 0.5}$/PDMS with a contact angle of 115°.

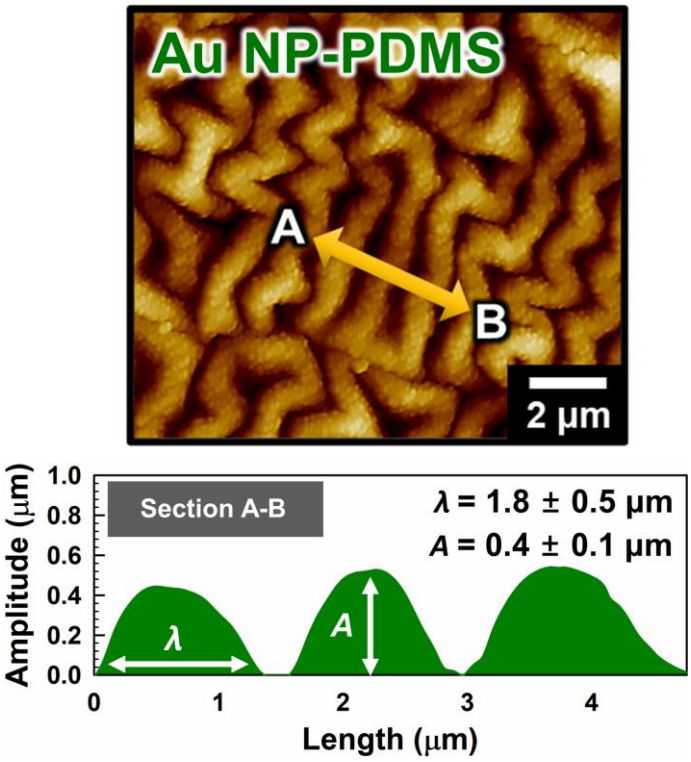

Figure S8. AFM topographic image (scan area = 12.5 μm × 12.5 μm) and cross-sectional height profile (obtained from Section A-B) of micro-wrinkled Au NP-PDMS with a wavelength of ~1.8 μm and an amplitude of ~0.4 μm.

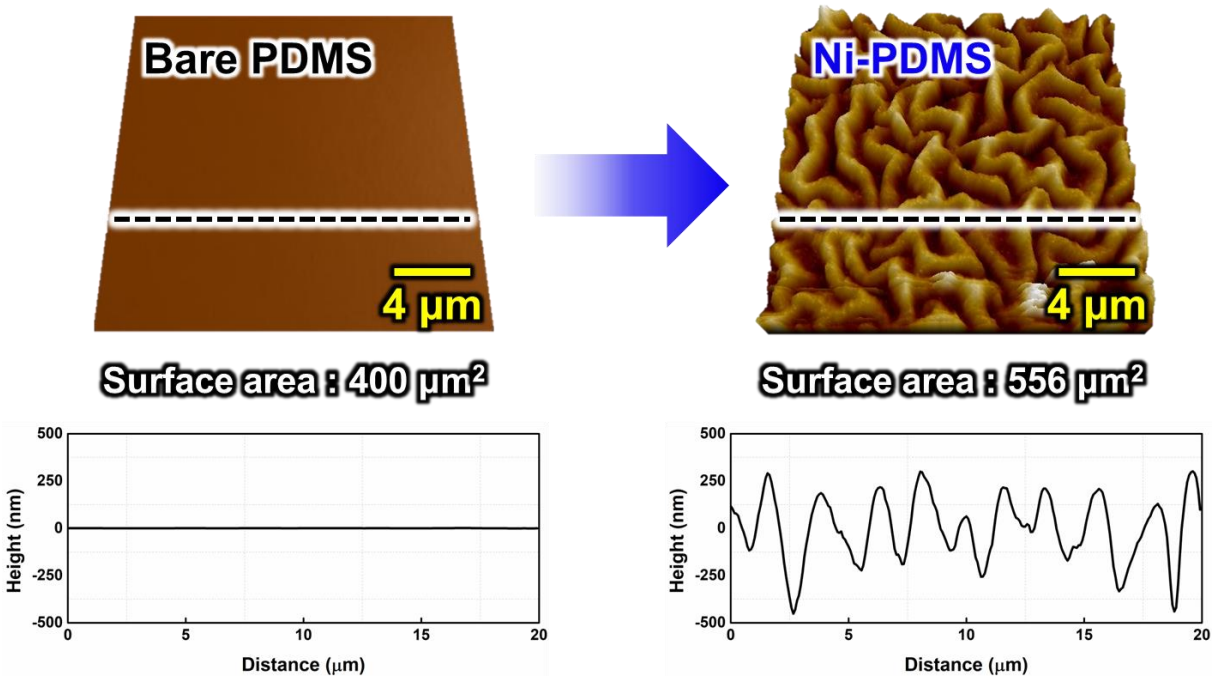

Figure S9. AFM topographic images (scan area = 20 μm × 20 μm) and cross-sectional height profile of bare PDMS elastomer and micro-wrinkled Ni-PDMS. The height profile was obtained from the black dashed lines in the AFM images. When the surface area was measured from the AFM measurements, the Ni-PDMS showed ~1.4 times higher surface area (~556 μm^2) than the bare PDMS elastomer (~400 μm^2), which was attributed to the formation of a micro-wrinkled structure.

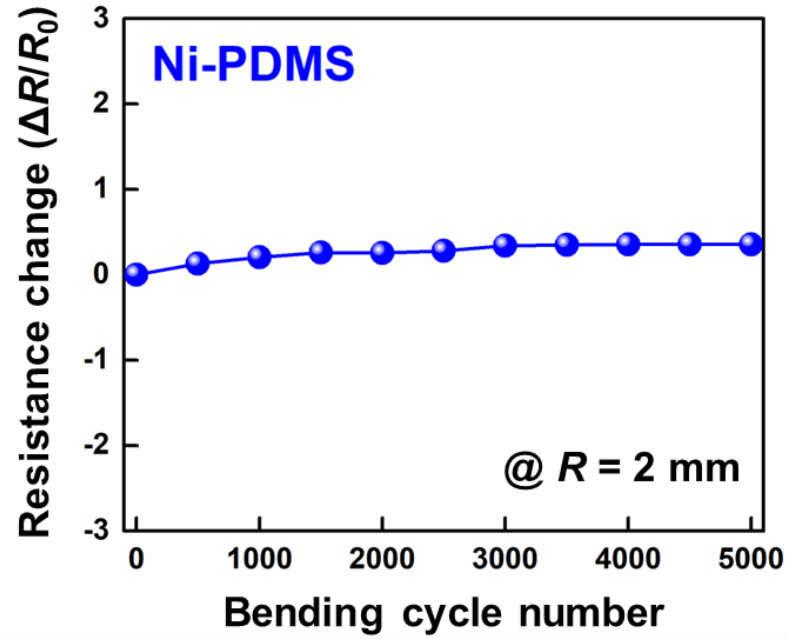

Figure S10. Resistance changes ($\Delta R/R_0$) of Ni-PDMS during 5000 bending cycles at the bending radius (R) of 2 mm.

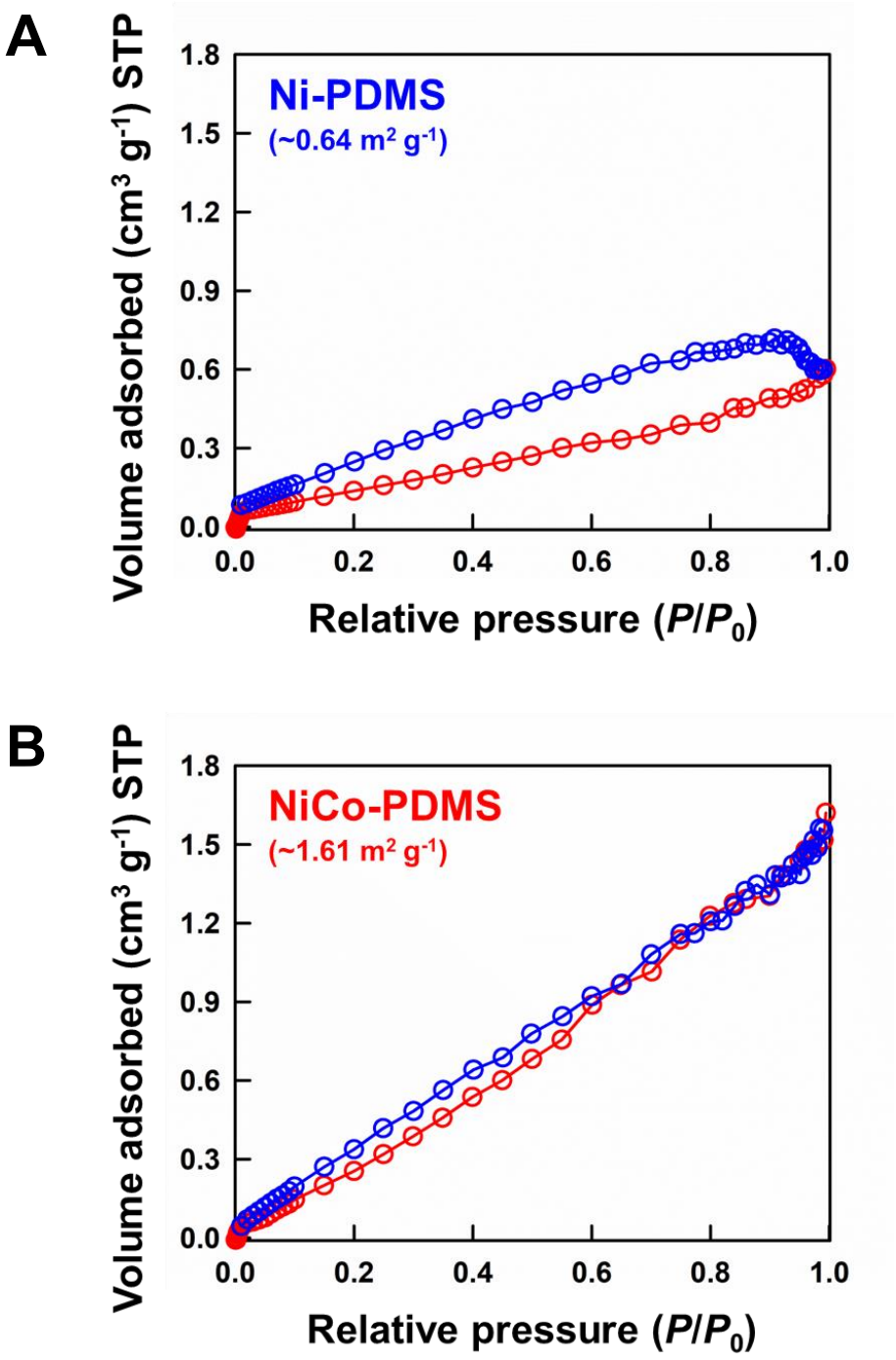

Figure S11. Nitrogen adsorption-desorption isotherms of (A) Ni-PDMS and (B) NiCo-PDMS, measured by Braunauer–Emmett–Teller (BET) analysis. In this case, the specific surface area of hierarchically micro/nano-wrinkled NiCo-PDMS was estimated to be ~1.61 m^2 g^{-1}, which was approximately 2.5 times higher compared to the micro-wrinkled Ni-PDMS (~0.64 m^2 g^{-1}).

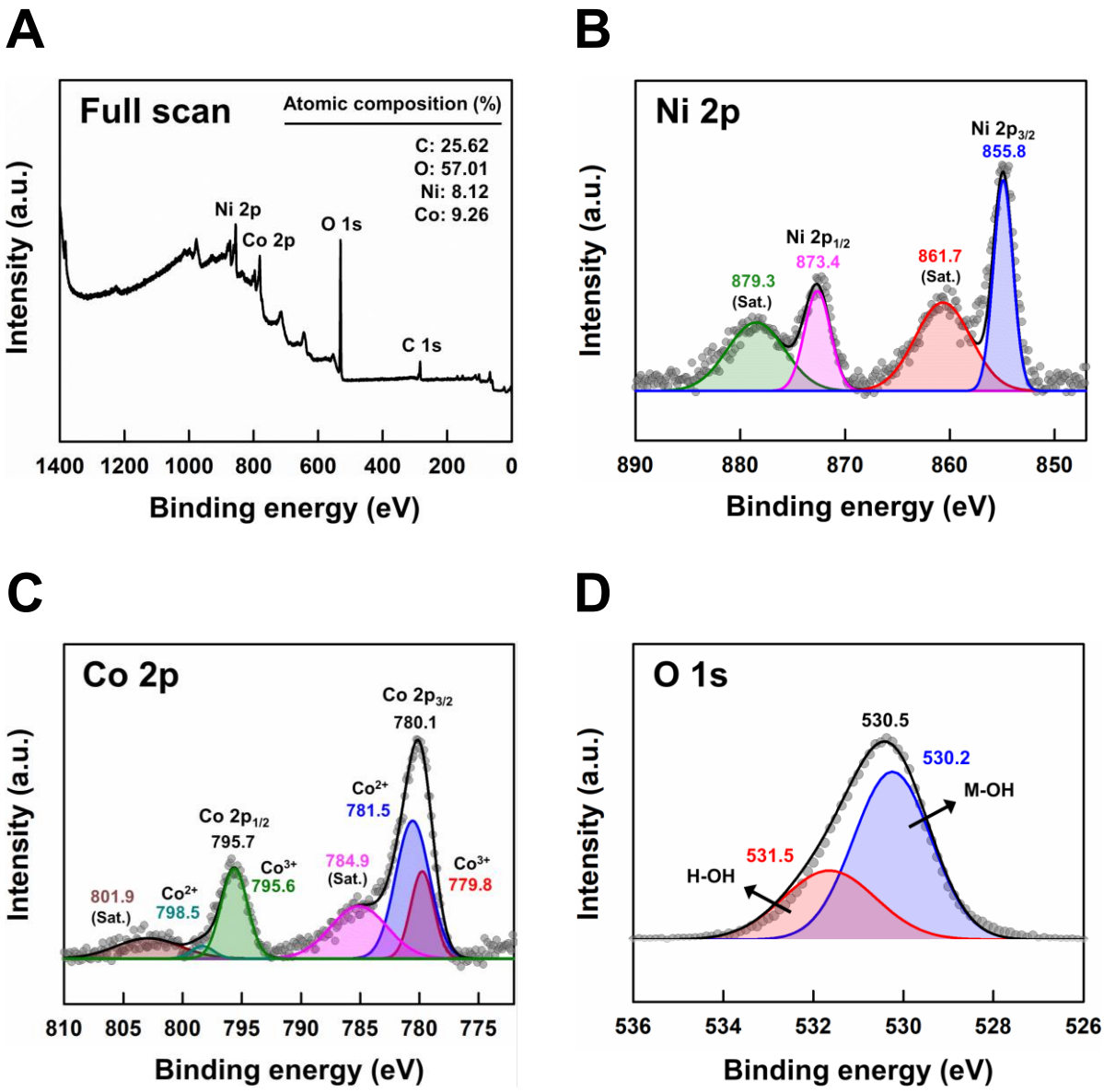

Figure S12. (A) Wide-survey XPS spectra of NiCo-PDMS. (B) Ni 2p, (C) Co 2p, and (D) O 1s core-level XPS spectra of NiCo-PDMS.

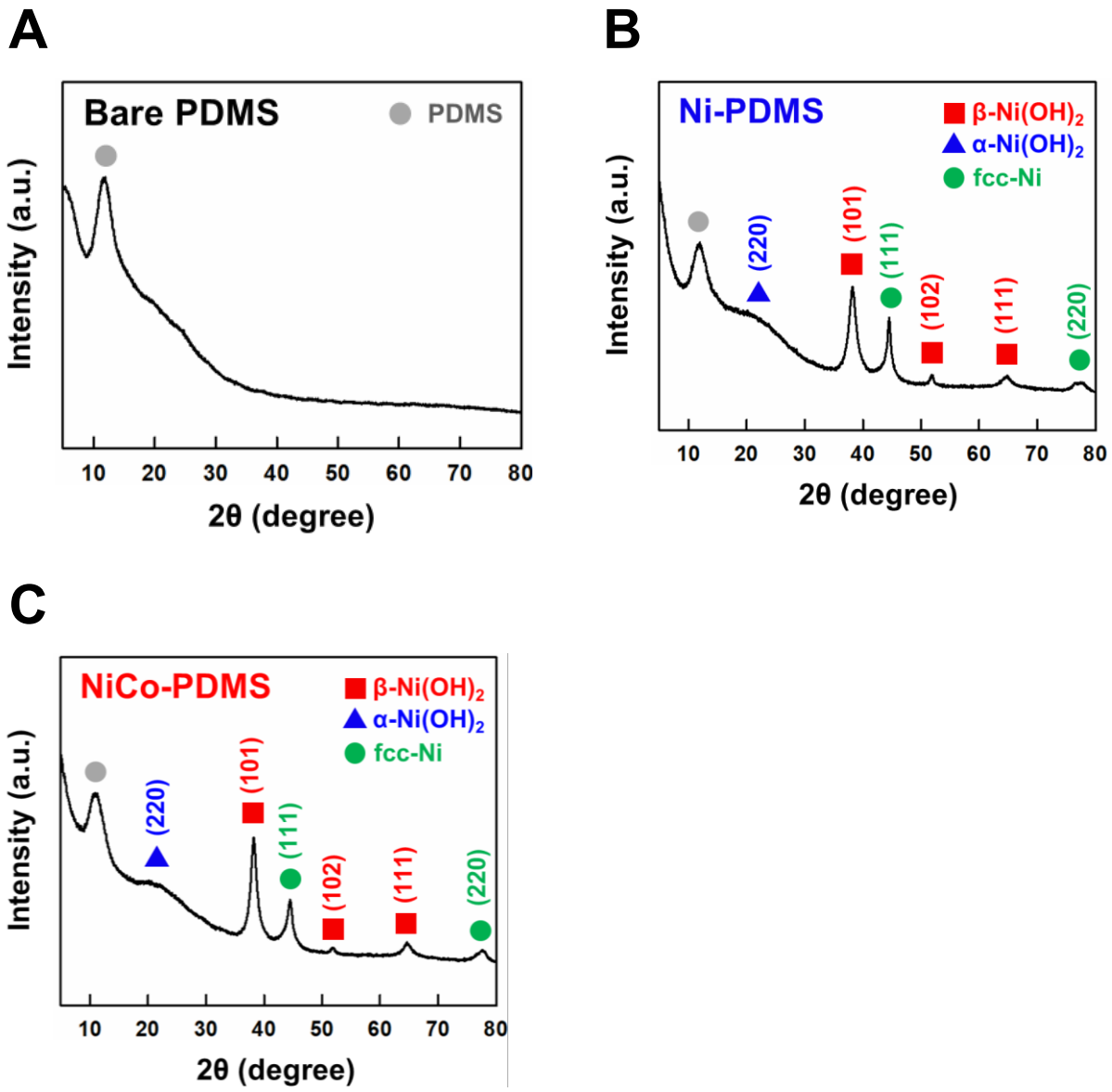

Figure S13. XRD patterns of (A) bare PDMS elastomer, (B) Ni-PDMS, and (C) NiCo-PDMS.

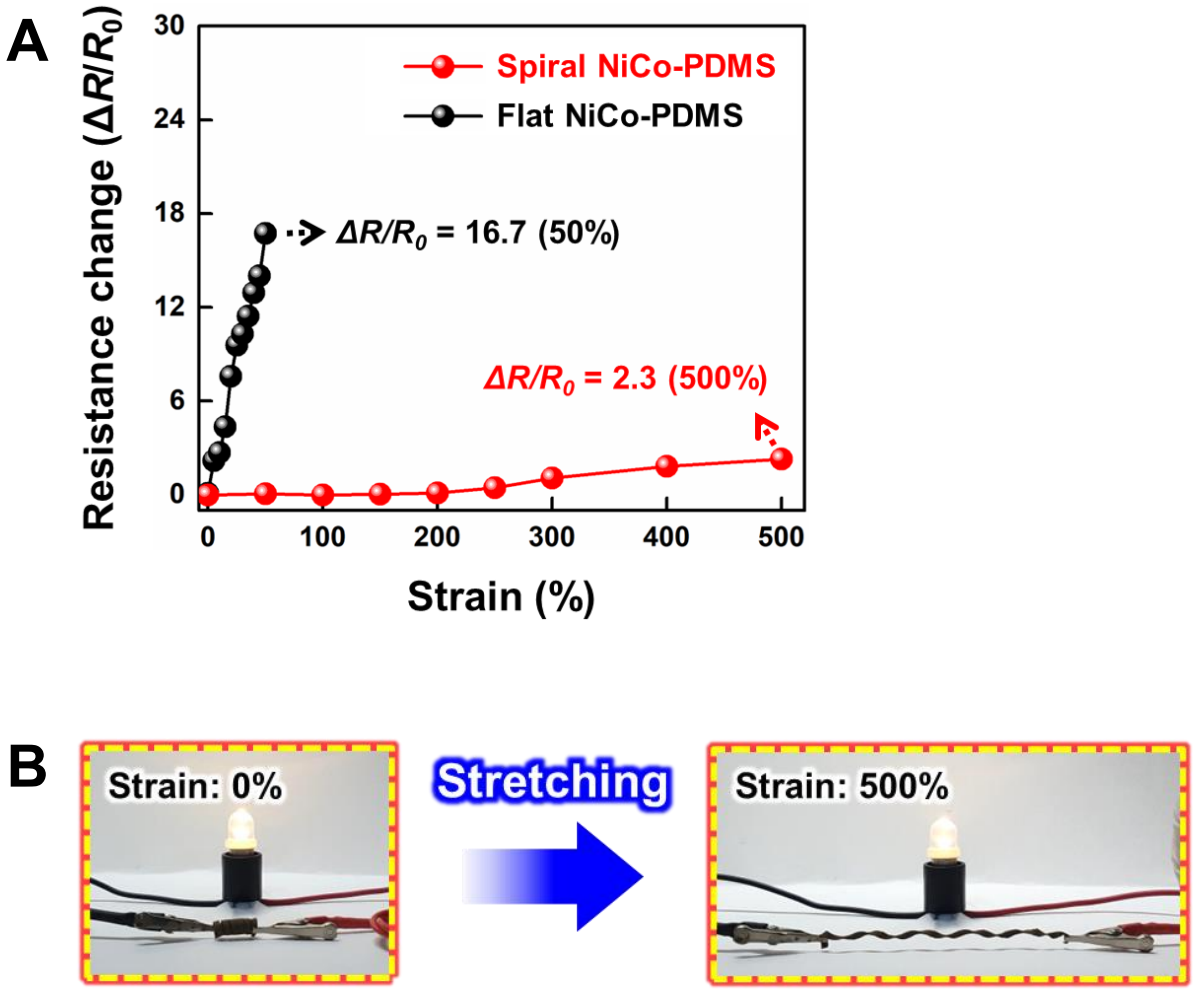

Figure S14. (A) Resistance changes ($\Delta R/R_0$) of spiral NiCo-PDMS and flat NiCo-PDMS with increasing the tensile strain from 0 to 500%. (B) Photographs of spiral NiCo-PDMS connected with light emitting diode (LED) at the initial (0%) and stretched (500%) states.

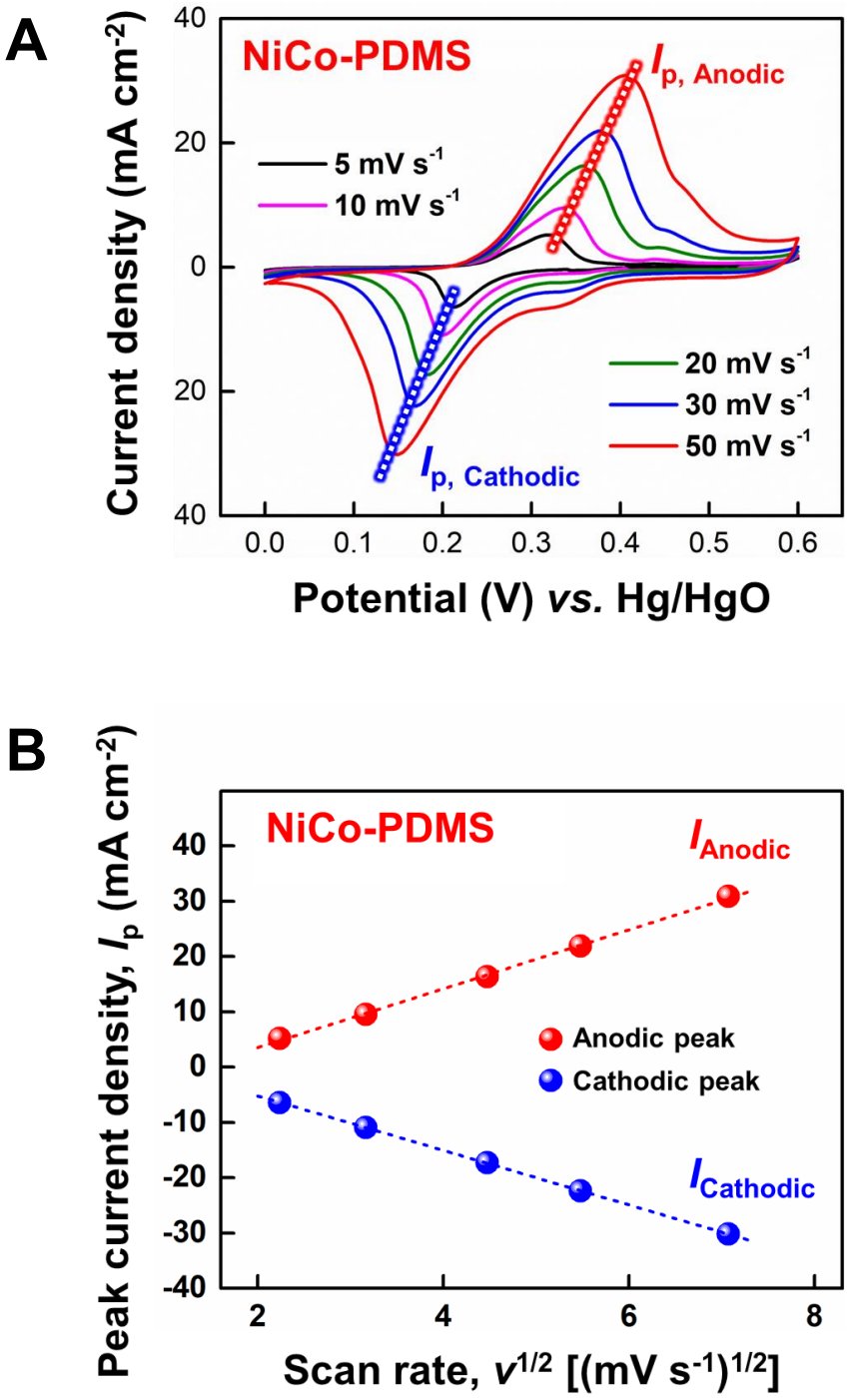

Figure S15. (A) Scan rate-dependent CV curves of NiCo-PDMS electrode in the range of 5 to 50 mV s^{-1}. (B) Square root of scan rate ($v^{1/2}$)-dependent cathodic/anodic peak current densities (I_p) from the CV curves of NiCo-PDMS electrode.

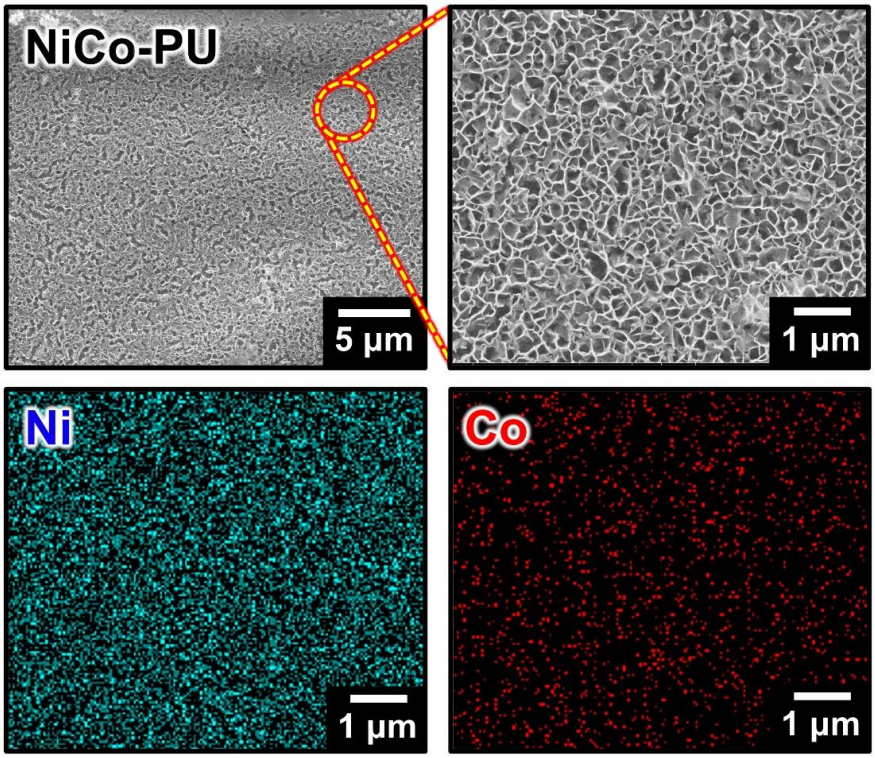

Figure S16. Planar FE-SEM images (top side) and corresponding EDX elemental mapping (Ni and Co; bottom side) of NiCo-PU. In this case, the NiCo-PU only showed the LDH-induced nanostrucure without any micro-wrinkled structure, in significant contrast to the hierarchically micro/nano-wrinkled NiCo-PDMS (see **Figure 2A**).

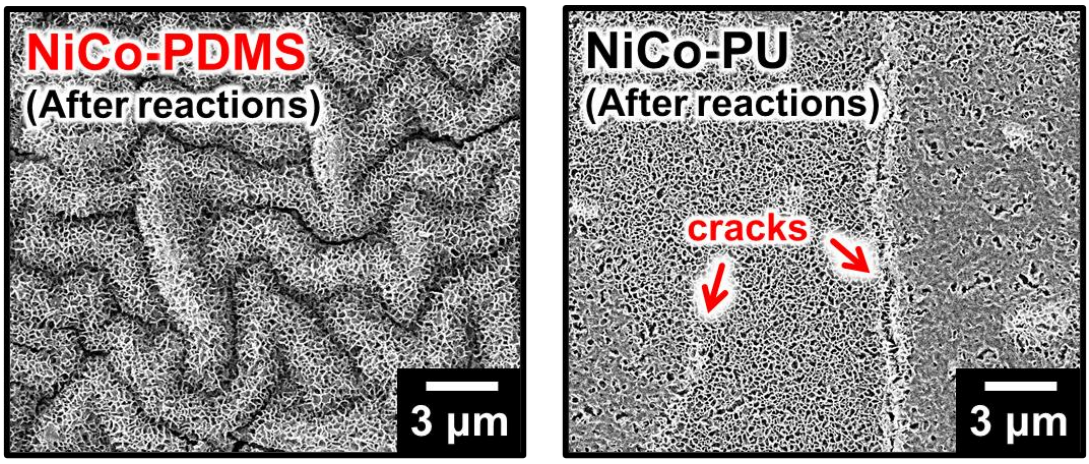

Figure S17. Planar FE-SEM images of NiCo-PDMS and NiCo-PU electrodes after repetitive electrochemical CV sweeps. In this case, the NiCo-PDMS electrode maintained its micro/nano-wrinkeld structures with well-interconnected conductive networks even after electrochemical sweeps. However, the NiCo-PU electrode with the only LDH-induced nanostructure underwent the irreversible structural failures (or cracks) after electrochemical sweeps.

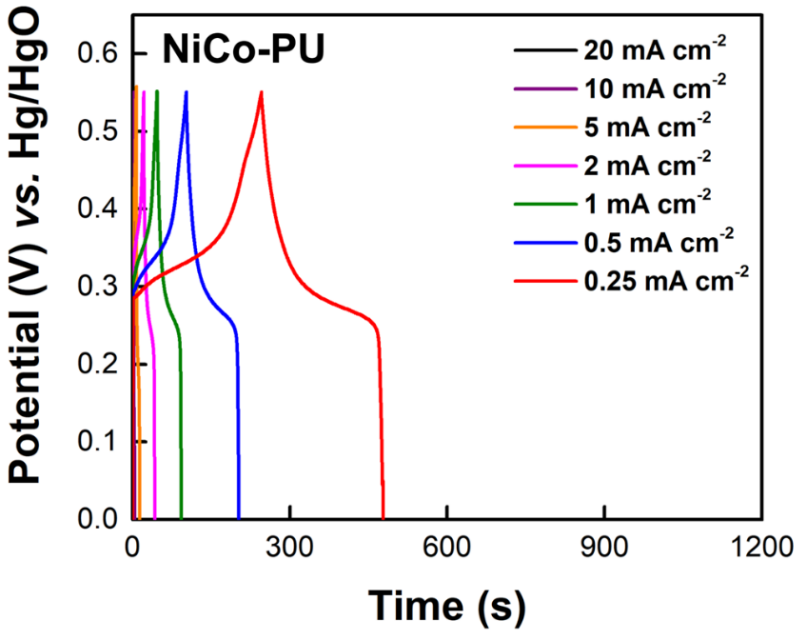

Figure S18. Current density-dependent GCD profiles of NiCo-PU electrodes in the range of 0.25 to 20 mA cm^{-2}.

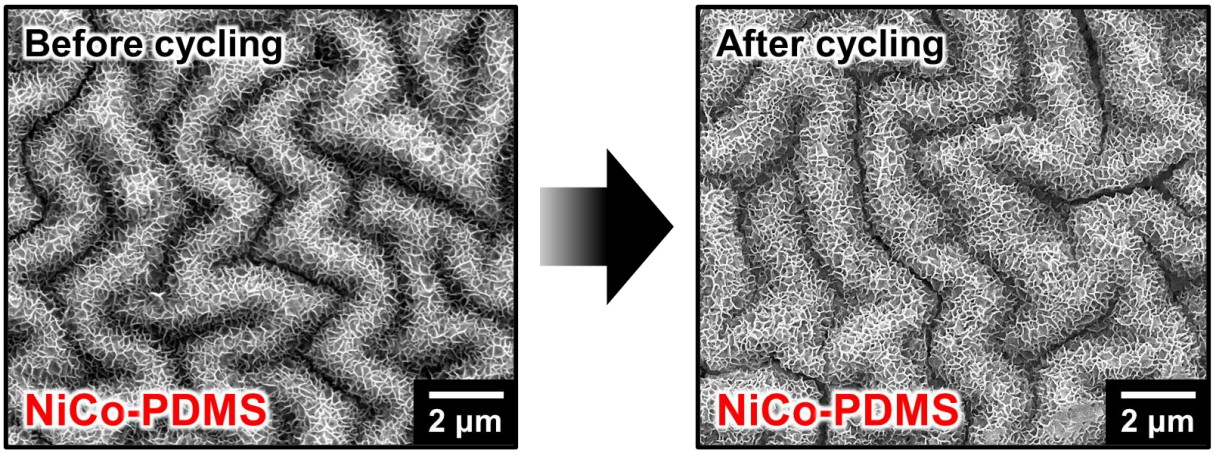

Figure S19. Planar FE-SEM images of NiCo-PDMS electrode before and after 5000 GCD cycles at a current density of 10 mA cm^{-2}.

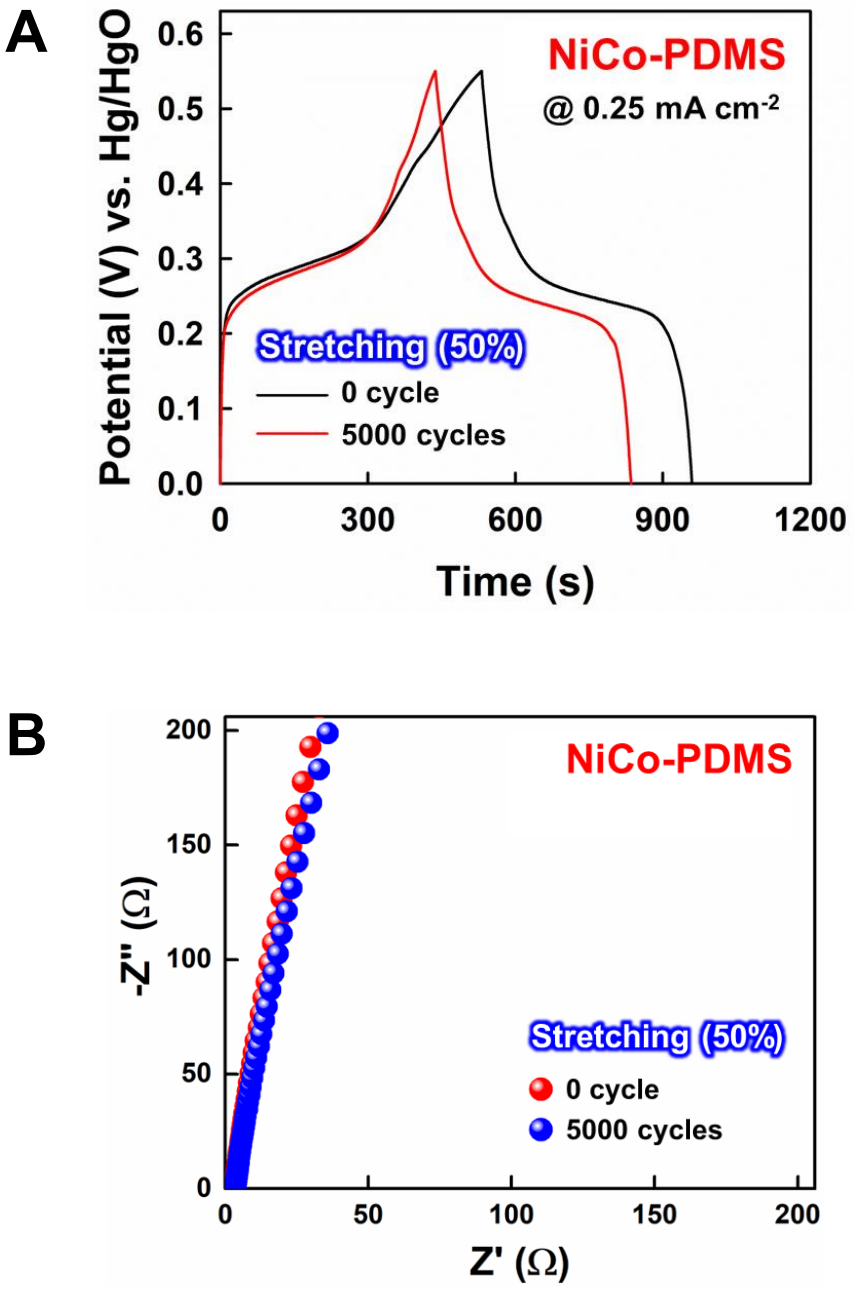

Figure S20. Comparison of (A) GCD curves at a current density of 0.25 mA cm^{-2} and (B) Nyquist plots between before and after 5000 stretching cycles at a tensile strain of 50%.

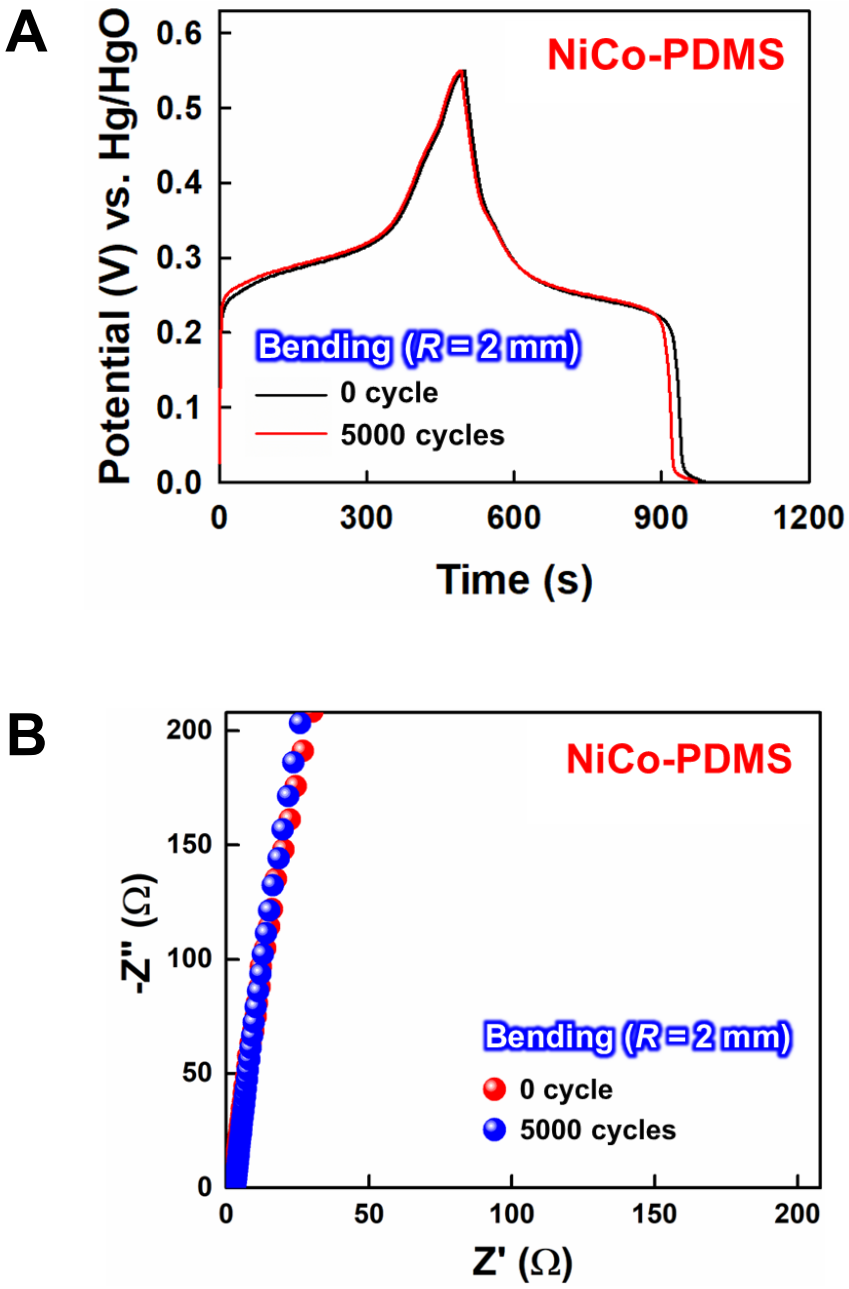

Figure S21. Comparison of (A) GCD curves at a current density of 0.25 mA cm^{-2} and (B) Nyquist plots between before and after 5000 bending cycles at a bending radius (R) of 2 mm.

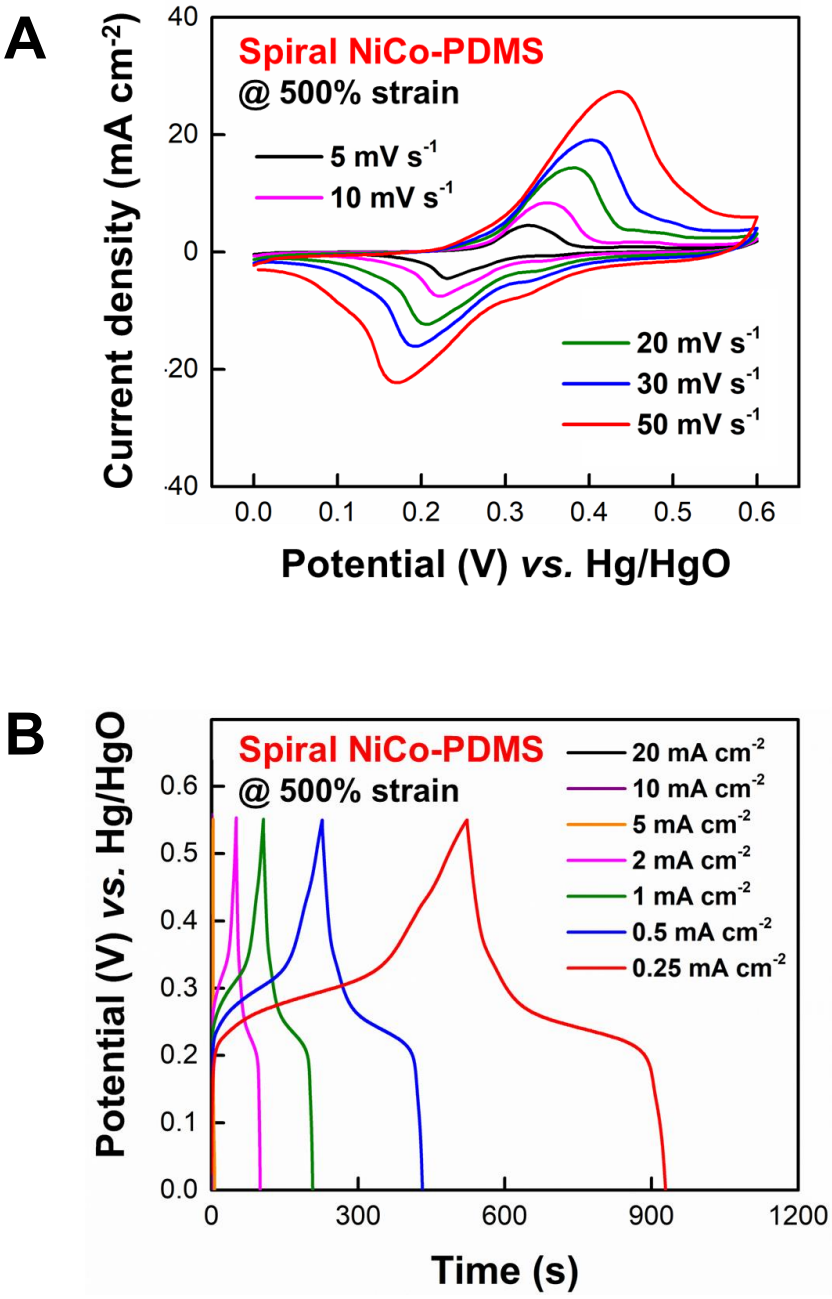

Figure S22. (A) Scan rate-dependent CV (in the range of 5 to 50 mV s^{-1}) and (B) current density-dependent GCD profiles (in the range of 0.25 to 20 mA cm^{-2}) of spiral NiCo-PDMS electrode at the stretched state of 500%.

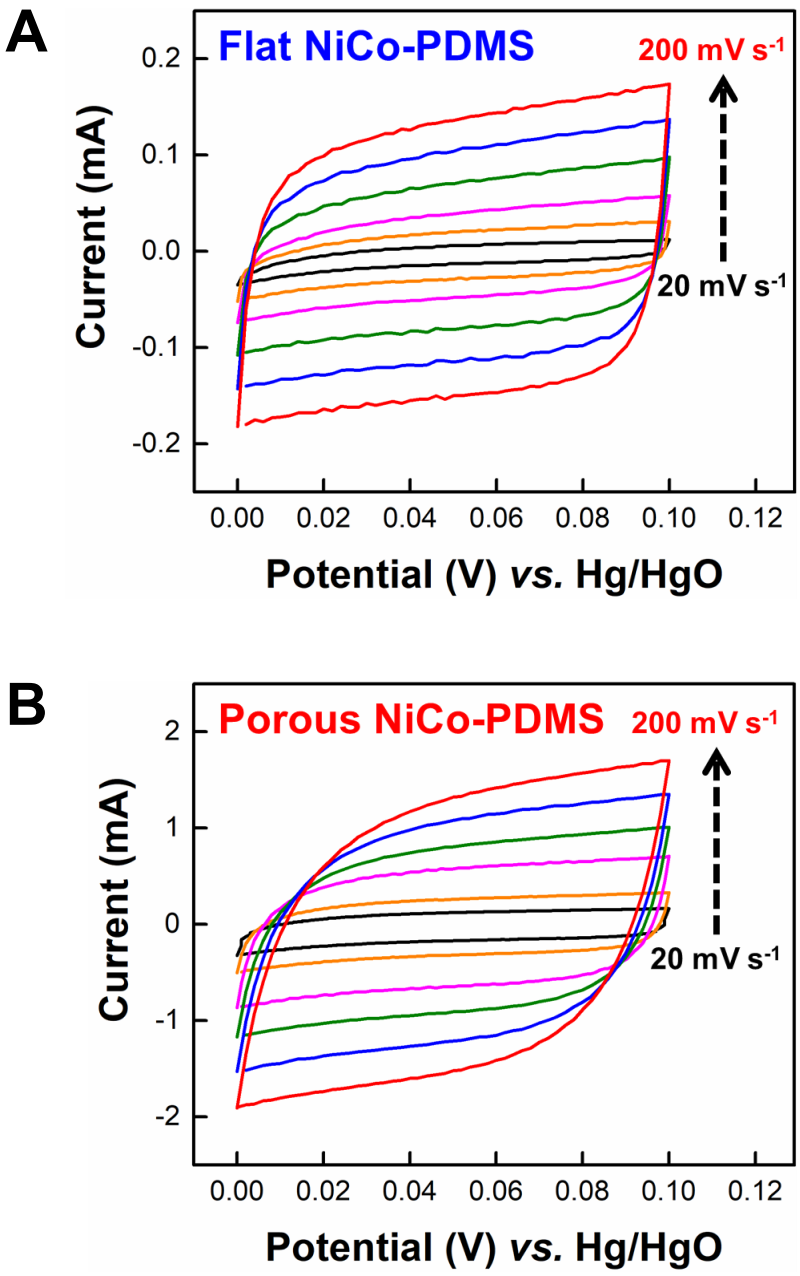

Figure S23. CV curves of (A) flat NiCo-PDMS and (B) porous NiCo-PDMS electrodes at varied scan rates ranging from 20 to 200 mV s^{-1} in the non-Faradaic potential region of 0 to 0.1 V.

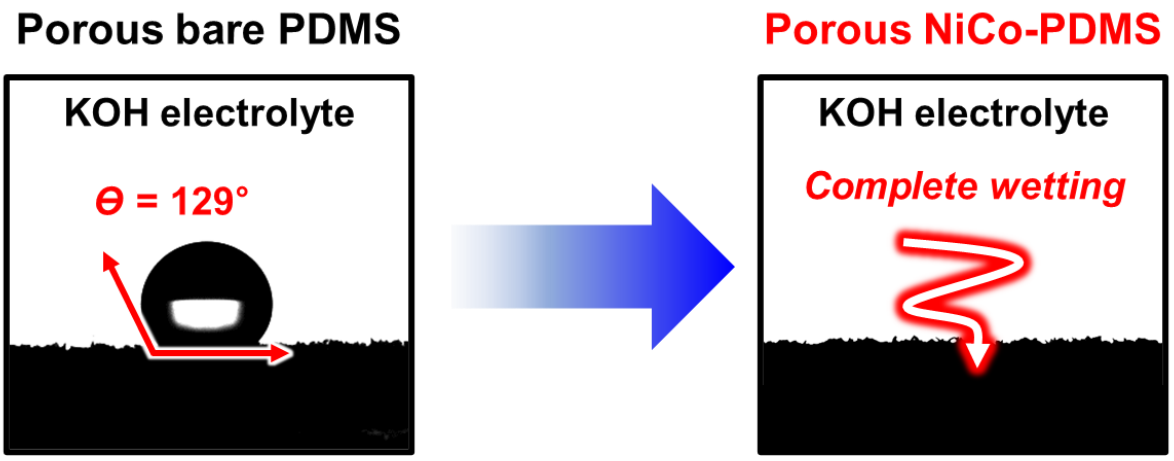

Figure S24. Photographs of KOH electrolyte droplets with cotact angles (θ) of porous bare PDMS elastomer and NiCo-PDMS. In this case, the porous bare PDMS elastomer showed hydrophobic surface properties with a contact angle of 129°, while the porous NiCo-PDMS showed complete wettability to the aqueous KOH electrolytes due to the conformal coating of a hydrophilic LDH layer from the exterior to the interior surface.

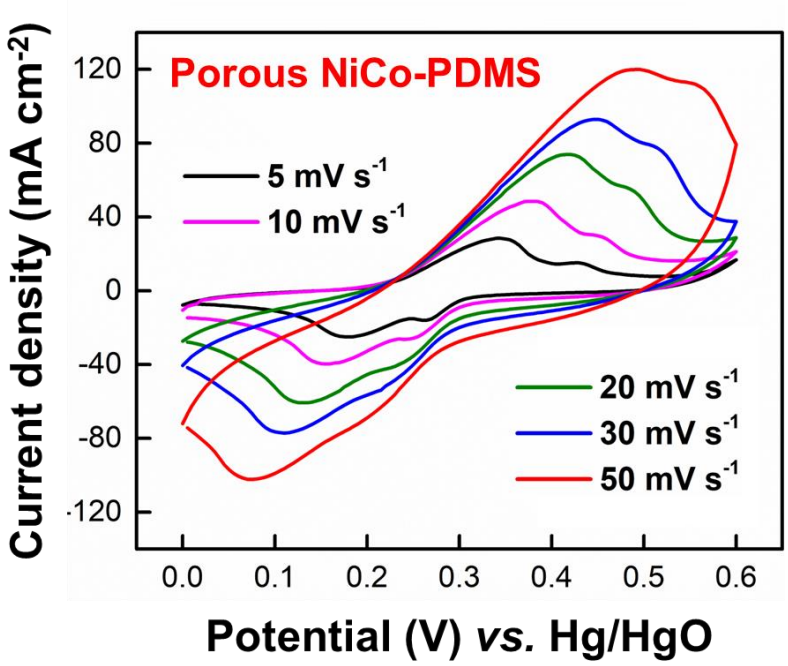

Figure S25. Scan rate-dependent CV curves of porous NiCo-PDMS electrode in the range of 5 to 50 mV s^{-1}.

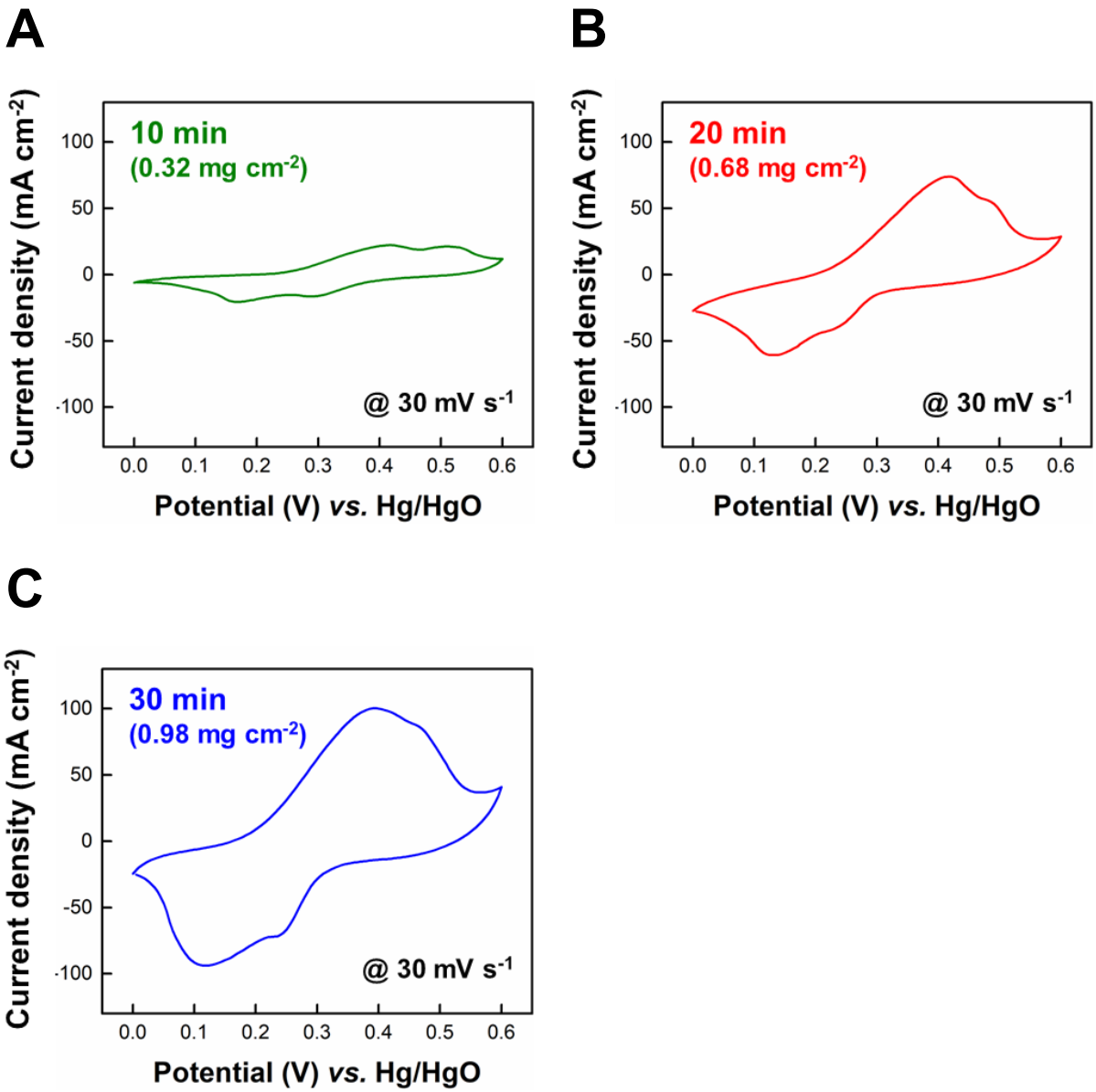

Figure S26. CV curves of porous NiCo-PDMS electrode at a scan rate of 30 mV s^{-1} with increasing the electrodeposition time (or mass loading) of NiCo LDH: (A) 10 min (~0.32 mg cm^{-2}), (B) 20 min (~0.68 mg cm^{-2}), (C) 30 min (~0.98 mg cm^{-2}).

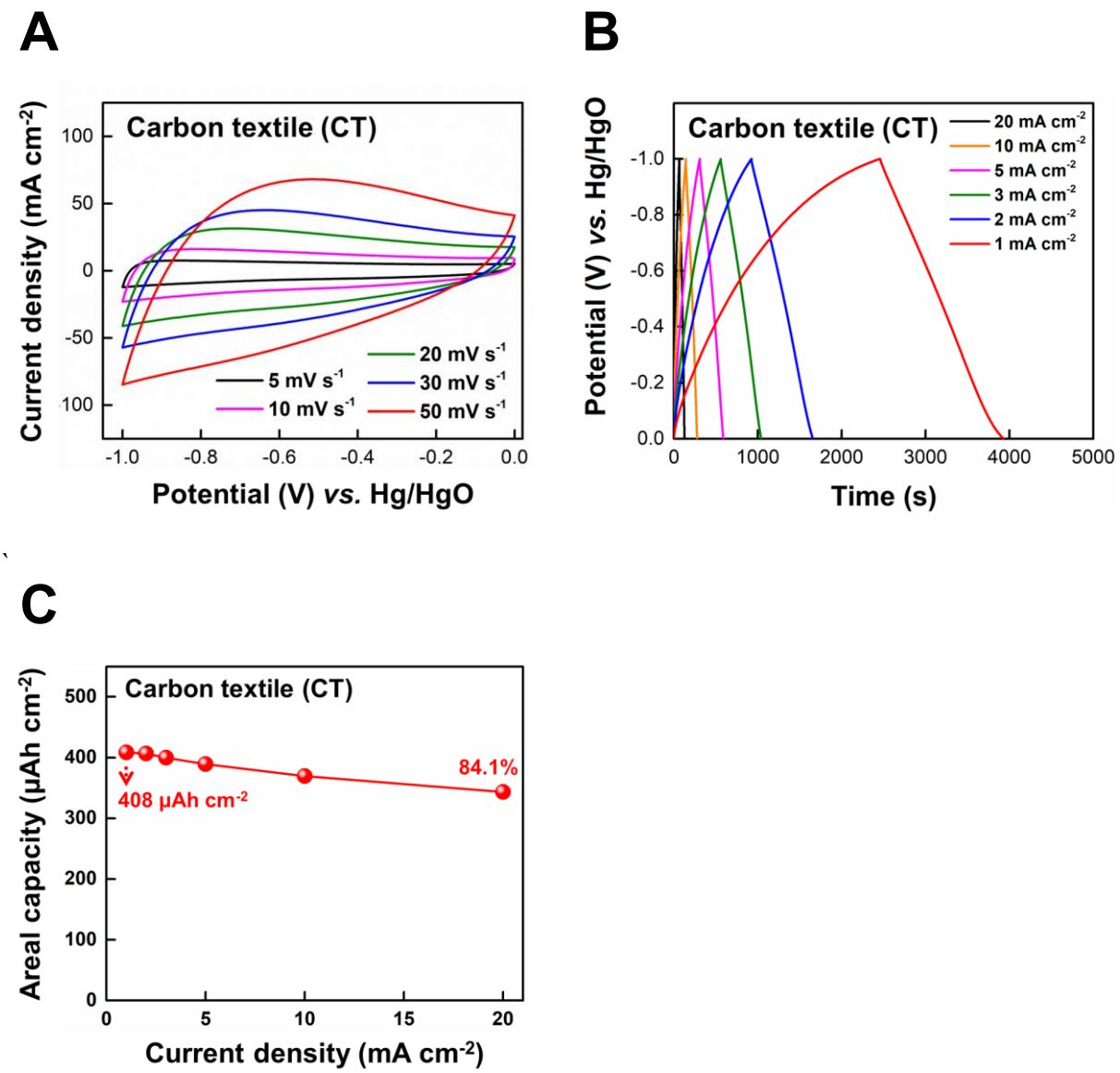

Figure S27. (A) Scan rate-dependent CV curves (in the range of 5 to 50 mV s^{-1}), (B) current density-dependent GCD curves (in the range of 1 to 20 mA cm^{-2}), and (C) areal capacity (obtained from GCD curves) of carbon textile (CT) electrode in a three-electrode system with a potential window of −1.0 to 0 V.

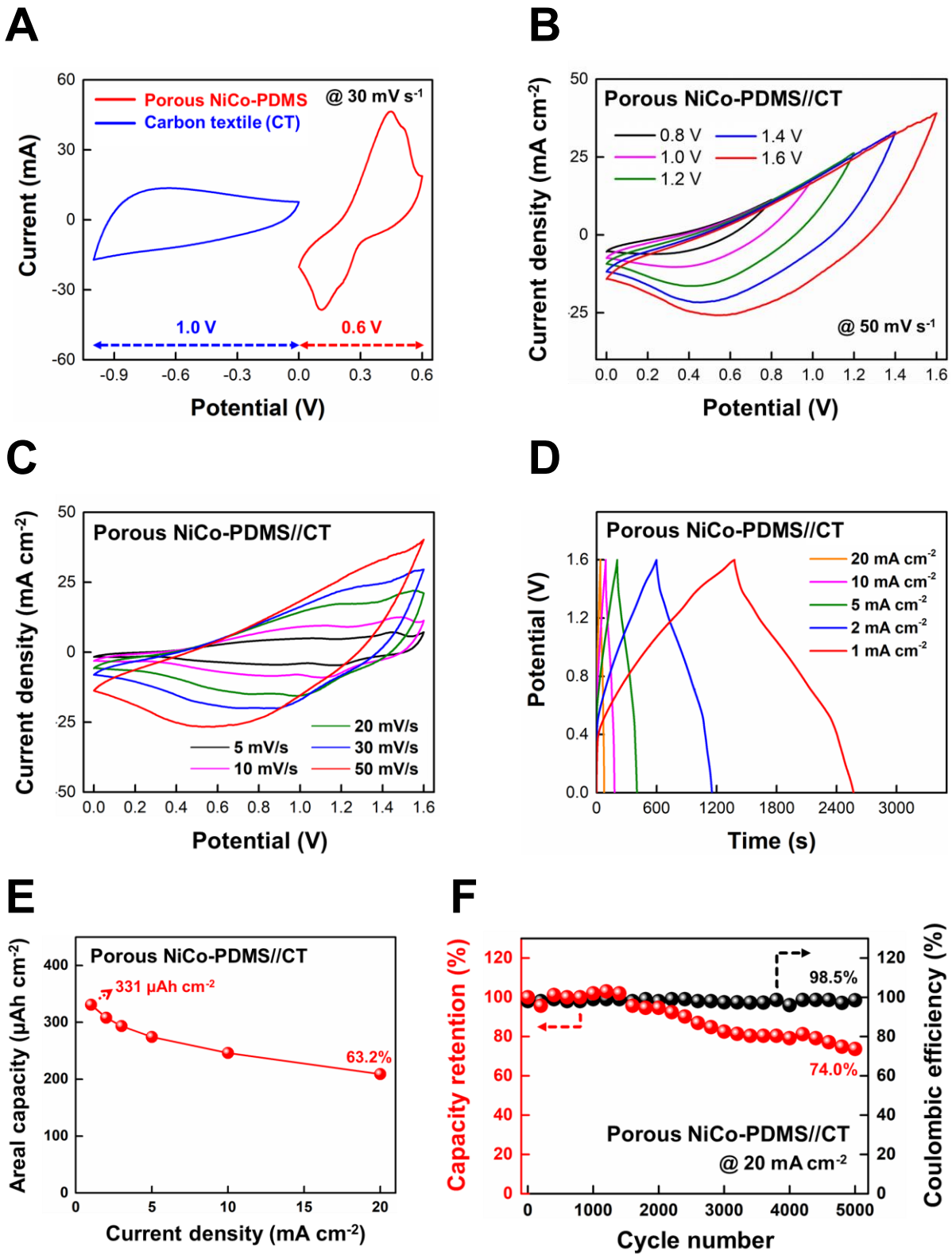

Figure S28. (A) CV curves of carbon textile (CT) electrode (in a potential window of −1.0 to 0 V) and porous NiCo-PDMS electrode (in a potential window of 0 to 0.6 V) at a scan rate of

30 mV s^{-1}. (B) CV curves of porous NiCo-PDMS//CT with increasing the overall potential window from 0.8 to 1.6 V at a scan rate of 50 mV s^{-1}. (C) Scan rate-dependent CV (in the range of 5 to 50 mV s^{-1}) and (D) current density-dependent GCD curves (in the range of 1 to 20 mA cm^{-2}) of porous NiCo-PDMS//CT. (E) Areal capacity of porous NiCo-PDMS//CT obtained from the GCD curves at different current densities ranging from 1 to 20 mA cm^{-2}. (F) Long-term cycling stability of porous NiCo-PDMS//CT during 5000 GCD cycles at a current density of 20 mA cm^{-2}.

Table S1. Comparison of electrical conductivities of elastomeric current collectors (ECCs).

Substrates	Conductive materials	Methods	Conductivity (S cm^{-1})	References
PDMS	**Ni**	**Metal NP Assembly-assisted electrodeposition**	**1.52×10^4**	**Our work**
Silicon rubber	CNT	[a)]FCCVD/Transfer	3.63×10^3	S11
PDMS	SWCNT	CVD/Transfer	2.00×10^3	S12
PDMS	Graphene	CVD/Transfer	1.25×10^3	S13
PU	[b)]CB/MWCNT	Blending	19.3	S14
PDMS	Au nanowire	Self-assembly/Transfer	*3.78×10^3	S15
PDMS	Au nanomesh	Grain boundary lithography/Transfer	*3.13×10^3	S16
PDMS	PEDOT:PSS /Ag nanowire	Spin coating/Spray coating	*3.14×10^3	S17
[c)]CPU	Ni flake/ [d)]EGaInPs	Stencil printing	2.48×10^3	S18

[a)]FCCVD: floating catalyst chemical vapor deposition, [b)]CB: carbon black, [c)]CPU: carboxylated polyurethane, [d)]EgaInPs: eutectic gallium indium particles

*Electrical conductivities were estimated from the given data in the literatures.

Table S2. Comparison of areal capacities of elastomeric energy storage electrodes.

Substrates	Active materials	Methods	Areal capacity (μAh cm^{-2})	References
PDMS	**NiCo**	**Metal NP assembly-assisted electrodeposition**	**280 @ 1mA cm^{-2}**	**Our work**
PDMS	PANI/[a]ACNTA	CVD-assisted electrodeposition	113 @ 1mA cm^{-2}	S19
Acrylic rubber	MXene/[b]CB	Nanocoating/Transfer	44 @ 1mA cm^{-2}	S20
PDMS/Ecoflex	Mn/Mo Oxide	Electrodeposition	4 @ 0.1 mA cm^{-2}	S21
PDMS	PANI/MWCNT	Water surface-assisted synthesis/Transfer	106 @ 5 mV s^{-1}	S22
PDMS	PANI/Graphene/CNT	CVD/Transfer	130 @ 0.4 mA cm^{-2}	S23
[c]EVA	PANI/CNT	Electrodeposition	124 @ 2 mA cm^{-2}	S24

[a]ACNTA: aligned carbon nanotube array, [b]CB: carbon black, [c]EVA: ethylene-vinyl acetate

Supporting References

S1 Brust M, Walker M, Bethell D, Schiffrin DJ, Whyman R. Synthesis of thiol-derivatised gold nanoparticles in a two-phase liquid-liquid system. *J. Chem. Soc. Chem. Commun.* 1994;(7):801-802.

S2 Zhang J, Chen Y, Brook MA. Facile functionalization of PDMS elastomer surfaces using thiol-ene click chemistry. *Langmuir.* 2013;29(40):12432-12442.

S3 Watts OP. Rapid nickel plating. *Trans. Am. Electrochem. Soc.* 1916;29:395-403.

S4 Nagaraju G, Raju GSR, Ko YH, Yu JS. Hierarchical Ni-Co layered double hydroxide nanosheets entrapped on conductive textile fibers: a cost-effective and flexible electrode for high-performance pseudocapacitors. *Nanoscale.* 2016;8(2):812-825.

S5 Won Y, Kim A, Yang W, Jeong S, Moon J. A highly stretchable, helical copper nanowire conductor exhibiting a stretchability of 700%. *NPG Asia Mater.* 2014;6:e132.

S6 Jang S, Min H, Cho SB, et al. A hierarchically tailored wrinkled three-dimensional foam for enhanced elastic supercapacitor electrodes. *Nano. Lett.* 2021;21(16):7079-7085.

S7 Park C, Lee T, Xia Y, Shin TJ, Myoung J, Jeong U. Quick, large-area assembly of a single-crystal monolayer of spherircal particles by unidirectional rubbing. *Adv. Mater.* 2014;26(27):4633-4638.

S8 Jang D, Kim Y, Kim TY, Koh K, Jeong U, Cho J. Force-assembled triboelectric nanogenerator with high-humidity-resistant electricity generation using hierarchical surface morphology. *Nano Energy.* 2016;20:283-293.

S9 Zhang S, Pan N. Supercapacitors performance evaluation. *Adv. Energy. Mater.* 2015;5(6):1401401.

S10 Turkevich J, Stevenson PC, Hiller J. A study of the nucleation and growth processes in the synthesis of colloidal gold. *Discuss. Faraday Soc.* 1951;11:55-75.

S11 Yu J, Lu W, Pei S, et al. Omnidirectionally stretchable high-performance supercapacitor based on isotropic buckled carbon nanotube films. *ACS Nano*. 2016;10(5):5204-5211.

S12 Niu Z, Dong H, Zhu B, et al. Highly stretchable, integrated supercapacitors based on single-walled carbon nanotube films with continuous reticulate architecture. *Adv. Mater.* 2013;25(7):1058-1064.

S13 Chen T, Xue Y, Roy AK, Dai L. Transparent and stretchable high-performance supercapacitors based on wrinkled graphene electrodes. *ACS Nano.* 2014;8(1):1039-1046.

S14 Mu H, Huang X, Wang W, Tian X, An Z, Wang G. High-Performance-Integrated stretchable supercapacitors based on a polyurethane organo/hydrogel electrolyte. *ACS Appl. Mater. Interfaces*. 2022;14(1):622-632.

S15 Gong S, Zhao Y, Shi Q, Wang Y, Yap LW, Cheng W. Self-assembled ultrathin gold nanowires as highly transparent, conductive and stretchable supercapacitor. *Electroanalysis.* 2016;28(6):1298-1304.

S16 Yang J, Hong T, Deng J, et al. Stretchable, transparent and imperceptible supercapacitors based on Au@MnO_2 nanomesh electrodes. *Chem. Commun.* 2019;55(91):13737-13740.

S17 Cai G, Park S, Cheng X, Eh ALS, Lee PS. Inkjet-printed metal oxide nanoparticles on elastomer for strain-adaptive transmissive electrochromic energy storage systems. *Sci. Technol. Adv. Mater.* 2018;19(1):759-770.

S18 Park S, Thangavel G, Parida K, Li S, Lee PS. A stretchable and self-healing energy storage device based on mechanically and electrically restorative liquid-metal particles and carboxylated polyurethane composites. *Adv. Mater.* 2019;31(1):1805536.

S19 Balboni RDC, Maron GK, Masteghin MG, et al. An easy to assemble PDMS/CNTs/PANI flexible supercapacitor with high energy-to-power density. *Nanoscale.* 2022;14(6):2266-2276.

S20 Chang TH, Zhang T, Yang H, et al. Controlled crumpling of two-dimensional titanium carbide (MXene) for highly stretchable, bendable, efficient supercapacitor. *ACS Nano.* 2018;12(8):8048-8059.

S21 Lee G, Kim JW, Park H, et al. Skin-like, dynamically stretchable, planar supercapacitors with buckled carbon nanotube/Mn-Mo mixed oxide electrodes and air-stable organic electrolyte. *ACS Nano.* 2019;13(1):855-866.

S22 Yu M, Zhang Y, Zeng Y, et al. Water surface assisted synthesis of large-scale carbon nanotube film for high-performance and stretchable supercapacitors. *Adv. Mater.* 2014;26(27):4724-4729.

S23 Liang X, Zhao L, Wang Q, Ma Y, Zhang D. A dynamic stretchable and self-healable supercapacitor with a CNT/graphene/PANI composite film. *Nanoscale.* 2018;10(47):22329-22334.

S24 Zhang Z, Zhang Y, Yang K, et al. Three-dimensional carbon nanotube/ethylvinlyacetate/polyaniline as a high performance electrode for supercapacitors. *J. Mater. Chem. A.* 2015;3(5):1884-1889.